Simulation of cohesive fine powders under a plane shear

Satoshi Takada,[1] Kuniyasu Saitoh,[2] and Hisao Hayakawa[1]
[1]*Yukawa Institute for Theoretical Physics, Kyoto University, Kitashirakawa Oiwakecho, Sakyo-ku, Kyoto 606-8502, Japan*
[2]*Faculty of Engineering Technology, MESA+, University of Twente, 7500 AE Enschede, The Netherlands*
(Received 6 December 2013; revised manuscript received 27 October 2014; published 29 December 2014)

Three-dimensional molecular-dynamics simulations of cohesive dissipative powders under a plane shear are performed. We find the various phases depending on the dimensionless shear rate and the dissipation rate as well as the density. We also find that the shape of clusters depends on the initial condition of velocities of particles when the dissipation is large. Our simple stochastic model reproduces the non-Gaussian velocity distribution function appearing in the coexistence phase of a gas and a plate.

DOI: 10.1103/PhysRevE.90.062207 PACS number(s): 45.70.Qj, 47.11.Mn, 64.70.F−, 83.10.Mj

I. INTRODUCTION

Fine powders, such as aerosols, volcanic ashes, flour, and toner particles are commonly observed in daily life. The attractive interaction between fine powders plays a major role [1–13], while there are various studies discussing the effects of cohesive forces between macroscopic powders [13–33]. For example, the Johnson-Kendall-Roberts theory describes the microscopic surface energy for the contact of cohesive grains [13,14]. The others study the attractive force caused by the liquid bridge for wet granular particles [27–33]. It should be noted that the cohesive force cannot be ignored for small fine powders. Indeed, the intermolecular attractive force always exists. Moreover, the inelasticity plays an important role when powders collide, because there are some excitations of internal vibrations, radiation of sounds, and deformations [34–43].

Let us consider cohesive powders under a plane shear. So far there exist many studies for one or two effects of the shear, an attractive force, and an inelastic collision [44–62], but we only know one example for the study of the jamming transition to include all three effects [63]. On the other hand, when the Lennard-Jones (LJ) molecules are quenched below the coexistence curve of gas-liquid phases [44–49], a phase ordering process proceeds after nucleation takes place [50–52]. It is well known that clusters always appear in freely cooling processes of granular gases [53–55]. Such clustering processes may be understood by a set of hydrodynamic equations of granular gases [56,57]. When we apply a shear to the granular gas, there exist various types of clusters such as the two-dimensional (2D) plug, 2D wave, or 3D wave for three-dimensional systems [58–62].

In this paper we try to characterize nonequilibrium pattern formation of cohesive fine powders under the plane shear by the three-dimensional molecular-dynamics (MD) simulations of the dissipative LJ molecules under the Lees-Edwards boundary condition [64]. In our previous paper [65] we mainly focused on the effect of dissipation on the pattern formation in Sllod dynamics [66,67]. In this study, we systematically study it by scanning a large area of parameter space to draw the phase diagrams with respect to the density, the dimensionless shear rate, and the dissipation rate without the influence of Sllod dynamics.

The organization of this paper is as follows. In the next section we introduce our model and setup for this study. Section III, the main part of this paper, is devoted to exhibiting the results of our simulation. In Sec. III A we show the phase diagrams for several densities, each of which has various distinct steady phases. We find that the system has a quasi-particle-hole symmetry. We also find that the steady states depend on the initial condition of velocities of particles when the dissipation is large. In Sec. III B we analyze the velocity distribution function and try to reproduce it by solving the Kramers equation with Coulombic friction under the shear. In Secs. IV and V we discuss and summarize our results, respectively. In Appendix A we study the pattern formation of the dissipative LJ system under the physical boundary condition. In Appendix B we illustrate the existence of Coulombic friction near the interface of the plate-gases coexistence phase. In Appendix C we demonstrate that the viscous heating term near the interface is always positive. In Appendix D we present a perturbative solution of the Kramers equation. In Appendix E we show the detailed calculations for each moment. In Appendix F we show the detailed calculations of the velocity distribution function.

II. MOLECULAR-DYNAMICS SIMULATION

In this section we explain our model and setup of the MD simulation for cohesive fine powders under a plane shear. We introduce our model of cohesive fine powders in Sec. II A and explain our numerical setup in Sec. II B.

A. Model

We assume that the interaction between two cohesive fine powders can be described by the LJ potential and an inelastic force caused by collisions with finite relative speeds. The explicit expression of the LJ potential is given by

$$U^{\mathrm{LJ}}(r_{ij}) = 4\varepsilon\Theta(r_{\mathrm{c}} - r_{ij})\left[\left(\frac{\sigma}{r_{ij}}\right)^{12} - \left(\frac{\sigma}{r_{ij}}\right)^{6}\right], \quad (1)$$

with a step function $\Theta(r) = 1$ and 0 for $r > 0$ and $r \leqslant 0$, respectively, where ε, σ, and r_{ij} are the well depth, the diameter of the repulsive core, and the distance between the particles i and j, respectively. Here we have introduced the cutoff length $r_{\mathrm{c}} = 3.0\sigma$ to save the computational cost, i.e., $U^{\mathrm{LJ}}(r) = 0$ for $r \geqslant r_{\mathrm{c}}$. To model the inelastic interaction, we introduce a viscous force between two colliding particles as

$$\boldsymbol{F}^{\mathrm{vis}}(\boldsymbol{r}_{ij}, \boldsymbol{v}_{ij}) = -\zeta\Theta(\sigma - r_{ij})(\boldsymbol{v}_{ij}\cdot\hat{\boldsymbol{r}}_{ij})\hat{\boldsymbol{r}}_{ij}, \quad (2)$$

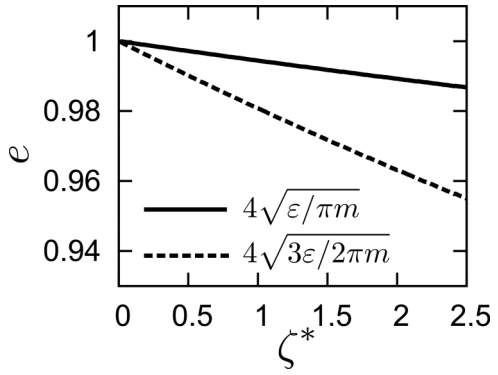

FIG. 1. Relationship between the dimensionless dissipation rate ζ^* and the coefficient of restitution e when the precollisional relative velocities are given by $4\sqrt{\varepsilon/\pi m}$ (solid line) and $4\sqrt{3\varepsilon/2\pi m}$ (dashed line).

where ζ, $\hat{\boldsymbol{r}}_{ij} \equiv \boldsymbol{r}_{ij}/r_{ij}$, and $\boldsymbol{v}_{ij} = \boldsymbol{v}_i - \boldsymbol{v}_j$ are the dissipation rate, a unit vector parallel to $\boldsymbol{r}_{ij} = \boldsymbol{r}_i - \boldsymbol{r}_j$, and the relative velocity between the particles, respectively. Here $\boldsymbol{r}_\alpha$ and $\boldsymbol{v}_\alpha$ ($\alpha = i, j$) are, respectively, the position and velocity of the particle. It should be noted that the range of inelastic interaction is only limited within the distance σ. From Eqs. (1) and (2) the force acting on the ith particle is given by

$$\boldsymbol{F}_i = -\sum_{j\neq i} \nabla_i U^{\mathrm{LJ}}(r_{ij}) + \sum_{j\neq i} \boldsymbol{F}^{\mathrm{vis}}(\boldsymbol{r}_{ij}, \boldsymbol{v}_{ij}). \tag{3}$$

Our LJ model has the advantage of knowing the detailed properties in equilibrium [44–49]. The normal restitution coefficient e, defined as the ratio of postcollisional speed to pre-collisional speed, depends on both the dissipation rate ζ and incident speed. For instance, the particles are nearly elastic, i.e., the restitution coefficient $e = 0.994$ for the case of $\zeta = \sqrt{\varepsilon/m\sigma^2}$ and the incident speed $\sqrt{\varepsilon/m}$, where m is the mass of each colliding particle. Figure 1 plots the restitution coefficient against the dimensionless dissipation rate $\zeta^* = \zeta\sqrt{m\sigma^2/\varepsilon}$, where the incident speeds are given by $4\sqrt{\varepsilon/\pi m}$ and $4\sqrt{3\varepsilon/2\pi m}$, respectively. We restrict the dissipation rate to small values in the range $0 < \zeta^* \leqslant 3.2$. Note that small and not too large inelasticity is necessary to reproduce a steady coexistence phase between a dense and a dilute region, which will be analyzed in detail in this paper. Indeed, the system cannot reach a steady state without inelasticity, while all particles are absorbed in a big cluster when inelasticity is large. In this paper we use three dimensionless parameters to characterize a system: the dimensionless density $n^* = n\sigma^3 = N\sigma^3/L^3$, the shear rate $\dot{\gamma}^* = \dot{\gamma}\sqrt{m\sigma^2/\varepsilon}$, and the dissipation rate $\zeta^* = \zeta\sqrt{m\sigma^2/\varepsilon}$. It should be noted that the well depth ε is absorbed in the dimensionless shear rate and the dissipation rate. Thus, we may regard the control of two independent parameters as the change of the well depth.

B. Setup

Figure 2 is a snapshot of our MD simulations for a uniformly sheared state, where we randomly distribute $N = 10^4$ particles in a cubic periodic box and control the number density n by adjusting the linear system size L. We first equilibrate

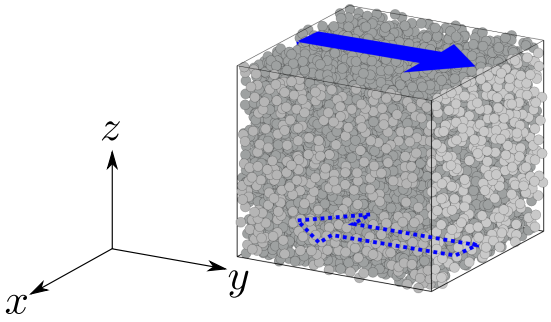

FIG. 2. (Color online) Snapshot of our simulation in a uniformly sheared state. We apply a plane shear in the xy plane, that is, we choose the y axis as the shear direction and the z axis as the velocity gradient direction.

the system by performing the MD simulations with the Weeks-Chandler-Andersen potential [68,69] during a time interval $100\sqrt{m\sigma^2/\varepsilon}$. We set the instance of the end of the initial equilibration process as the origin of the time for later discussion. Then we replace the interaction between the particles by the truncated LJ potential (1) with the dissipation force (2) under the Lees-Edwards boundary condition. As shown in Appendix A, the results under the Lees-Edwards boundary condition are almost equivalent to those under the flat boundary. The time evolution of position $\boldsymbol{r}_i = (x_i, y_i, z_i)$ is given by Newton's equation of motion $md^2\boldsymbol{r}_i/dt^2 = \boldsymbol{F}_i$.

III. RESULTS

In this section we present the results of our MD simulations. In Sec. III A we draw phase diagrams of the spatial structures of cohesive fine powders. In Sec. III B we present the results of velocity distribution functions and reproduce it by solving a phenomenological model.

A. Phase diagram

Figure 3 displays typical patterns formed by the particles in their steady states, which are characterized by the dimensionless parameters n^*, $\dot{\gamma}^*$, and ζ^* as listed in Table I. Figure 4 shows phase diagrams in the steady states for (a) $n^* = 0.0904$, (b) $n^* = 0.156$, (c) $n^* = 0.305$, and (d) $n^* = 0.723$. Three of these phases, those in Figs. 3(a), 3(d), and 3(g), are similar to those observed in a quasi-two-dimensional case with Sllod dynamics [70]. If the shear is dominant, the system remains in a uniformly sheared phase [Fig. 3(a)]. However, if the viscous heating by the shear is comparable to the energy dissipation, we find that a spherical droplet, a dense cylinder, and a dense plate coexist for extremely dilute ($n^* = 0.0904$), dilute ($n^* = 0.156$), and moderately dense ($n^* = 0.305$) gases, respectively [Figs. 3(b)–3(d)]. These three coexistence phases are realized by the competition between the equilibrium phase transition and the dynamic instability caused by inelastic collisions. Furthermore, if the energy dissipation is dominant, there are no gas particles in steady states [Figs. 3(e)–3(g)]. For an extremely-high-density case ($n^* = 0.723$), we observe an inverse cylinder, where the vacancy forms a hole passing through the dense region along the y axis [Fig. 3(h)], and an inverse droplet, where the shape of the vacancy is spherical

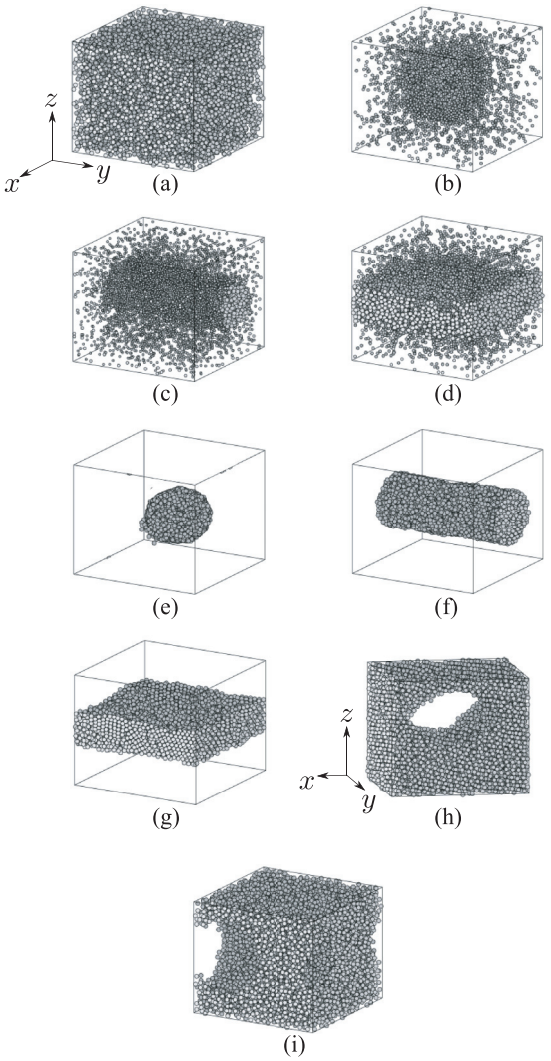

FIG. 3. Steady patterns made of the particles under the plane shear: (a) the uniformly sheared phase, (b) coexistence of a spherical droplet and gas, (c) coexistence of a dense cylinder and gas, (d) coexistence of a dense plate and gases, (e) an isolated spherical droplet, (f) an isolated dense cylinder, (g) an isolated dense plate, (h) an inverse cylinder, and (i) an inverse droplet, where the corresponding dimensionless parameters n^*, $\dot{\gamma}^*$, and ζ^* for (a)–(i) are listed in Table I. We note that gas particles in (b)–(d) are drawn smaller than the real size for visibility.

TABLE I. Dimensionless parameters used in Fig. 3.

Phase	n^*	$\dot{\gamma}^*$	ζ^*
(a)	0.305	10^{-1}	10^{-2}
(b)	0.0904	$10^{-0.5}$	$10^{0.5}$
(c)	0.156	$10^{-0.5}$	10^{0}
(d)	0.305	$10^{-0.2}$	$10^{0.2}$
(e)	0.0904	10^{-2}	10^{-1}
(f)	0.156	10^{-1}	$10^{-0.75}$
(g)	0.305	10^{-1}	10^{-1}
(h)	0.723	10^{-2}	10^{-1}
(i)	0.723	10^{-2}	10^{-2}

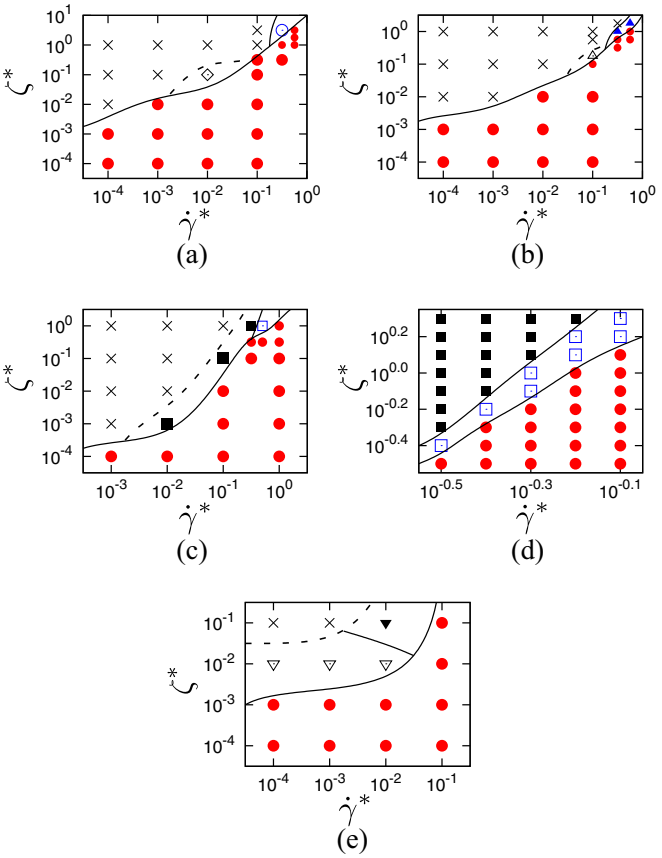

FIG. 4. (Color online) Phase diagrams for various densities, where the dimensionless densities are given by (a) $n^* = 0.0463$, (b) $n^* = 0.156$, (c) $n^* = 0.305$, and (d) $n^* = 0.305$ for $10^{-0.5} \leqslant \dot{\gamma}^* \leqslant 10^{-0.1}$ and (e) $n^* = 0.723$. The spatial patterns corresponding to Figs. 3(a)–3(i) are represented by red closed circles [Fig. 3(a)], blue open circle [Fig. 3(b)], blue closed up triangles [Fig. 3(c)], blue open squares [Fig. 3(d)], black open diamond [Fig. 3(e)], black open up triangle [Fig. 3(f)], black closed squares [Fig. 3(g)], black closed down triangle [Fig. 3(h)], and black open down triangles Fig. 3(i), respectively. The steady states represented by the crosses show various patterns depending on the initial velocities of particles.

[Fig. 3(i)]. In our simulation, the role of particles in a dilute system corresponds to that of vacancies in a dense system. Thus, the system has a quasi-particle-hole symmetry.

Moreover, the shape of clusters depends on the initial condition of the velocities of particles, even though a set of parameters such as the density, the shear rate, the dissipation rate, and the variance of the initial velocity distribution function is identical when the dissipation is strong. We observe a dense plate parallel to the xy plane [Fig. 5(a)], a dense plate parallel to the yz plane [Fig. 5(b)], and a dense cylinder parallel to the y axis [Fig. 5(c)] under the identical set of parameters. This initial velocity dependence appears in the region far from the coexistence phases, where the system evolves from aggregates of many clusters (see Fig. 6).

B. Velocity distribution function

We also measure the velocity distribution function (VDF) $P(u_i)$ $(i = x, y, z)$, where u_i is the velocity fluctuation around the mean velocity field $\bar{v}_i$ averaged over time and different

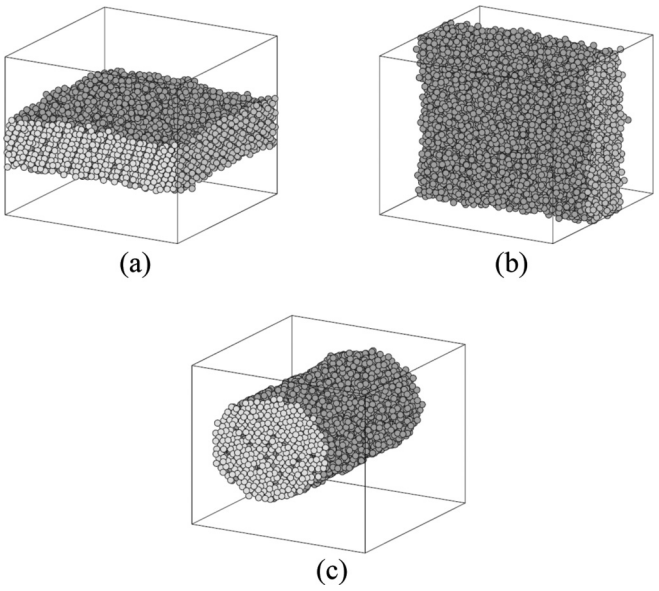

FIG. 5. Typical examples of the initial configuration dependence when we start from identical parameters ($n^* = 0.305$, $\dot{\gamma}^* = 10^{-3}$, and $\zeta^* = 10^{-2}$): (a) a dense-plate cluster parallel to the xy plane, (b) a dense-plate cluster parallel to the yz plane, and (c) a dense-cylinder cluster parallel to the x axis.

samples in the steady state. For simplicity, we focus only on the following three phases: the uniformly sheared phase [Fig. 3(a)], the dense-plate coexistence phase [Fig. 3(d)], and the dense-plate cluster phase [Fig. 3(g)]. In this paper we use the width $\Delta z = \sigma$ for bins in the z direction, while the bin sizes in both the x and y directions are L to evaluate the VDF from our MD simulations as in Fig. 7. It is remarkable that the VDF is almost an isotropic Gaussian function for the phases corresponding to Figs. 3(a) and 3(g) as well as deep

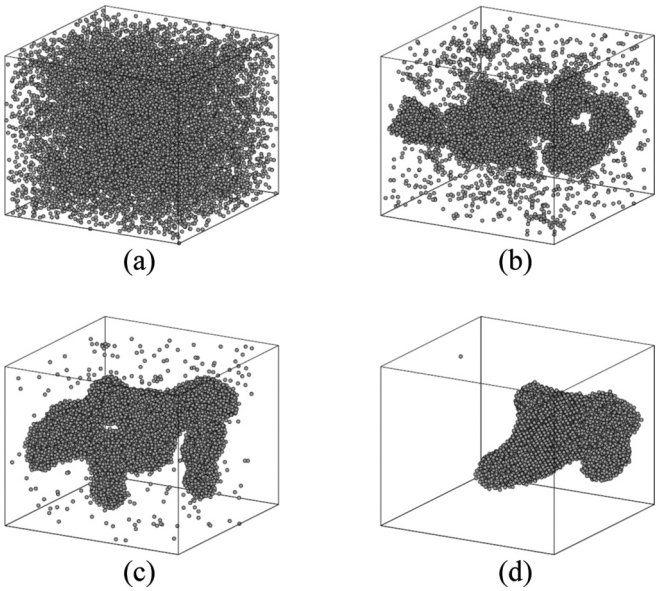

FIG. 6. Time evolution of configurations for $n^* = 0.0904$, $\dot{\gamma}^* = 10^{-1}$, and $\zeta^* = 10^{0.5}$ at (a) $t^* = 0$, (b) $t^* = 50$, (c) $t^* = 100$, and (d) $t^* = 550$.

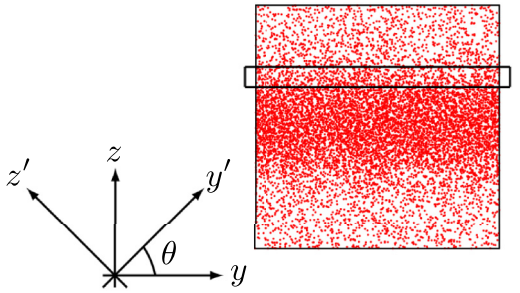

FIG. 7. (Color online) Snapshot of our simulation for the plate-gas coexistence phase. Solid lines refer to the edges of a bin. The binwise velocity distribution function is calculated in each bin, whose width is $\Delta z = \sigma$. In addition, we introduce a new coordinate (y', z') and θ, which is the angle between the y' and y directions (in the counterclockwise direction) for later analysis.

inside both the dense and the gas regions in the coexistence phase in Fig. 3(d) [see Figs. 8(a)–8(d)]. This is because we are interested in weak shear and weak dissipation cases without the influence of gravity. On the other hand, the VDF is nearly equal to an anisotropic exponential function [71,72] in the vicinity of the interface between the dense and the gas regions in the coexistence phase corresponding to Fig. 3(d) as in Figs. 8(e)–8(g). We now explain the non-Gaussian feature near the interface by a simple stochastic model of a tracer particle subjected to Coulombic friction (the justification to use such a model is explained in Appendix B). Let us consider a situation in which a gas particle hits and slides on the wall formed by the particles in the dense region (see Fig. 9). Because the velocity gradient in the gas region is almost constant as shown in Fig. 10, we may assume that a tracer particle in the gas near the interface is affected by a plane shear. Moreover, the tracer particle on a dense region may be influenced by Coulombic friction (see Appendix B). When we assume that the collisional force among gas particles can be written as the Gaussian random noise ξ, the equations of motion of a tracer particle at the position $\boldsymbol{r}$ may be given by

$$\frac{d\boldsymbol{r}}{dt} = \frac{\boldsymbol{p}}{m} + \dot{\gamma} z \hat{\boldsymbol{e}}_y, \tag{4}$$

$$\frac{d\boldsymbol{p}}{dt} = -\mu F_0 \frac{\boldsymbol{p}}{|\boldsymbol{p}|} - \dot{\gamma} p_z \hat{\boldsymbol{e}}_y + \boldsymbol{\xi}, \tag{5}$$

where $\boldsymbol{p}$ is a peculiar momentum, which is defined by Eq. (4). Here we have introduced the friction constant μ_0 and the effective force F_0, which is a function of the activation energy ΔE from the most stable trapped configuration of the solid crystal (see Fig. 9). Here ξ is assumed to satisfy

$$\langle \xi_\alpha(t) \rangle = 0, \quad \langle \xi_\alpha(t) \xi_\beta(t') \rangle = 2D\delta_{\alpha,\beta}\delta(t - t'), \tag{6}$$

where $\langle \cdots \rangle$ is the average over the distribution of the random variable $\boldsymbol{\xi}$ and D is the diffusion coefficient in the momentum space, which satisfies the fluctuation-dissipation relation $D = \mu F_0 \sqrt{mT/(d+1)}$ in the d-dimensional system with a temperature T. A set of Langevin equations (4) and (5)

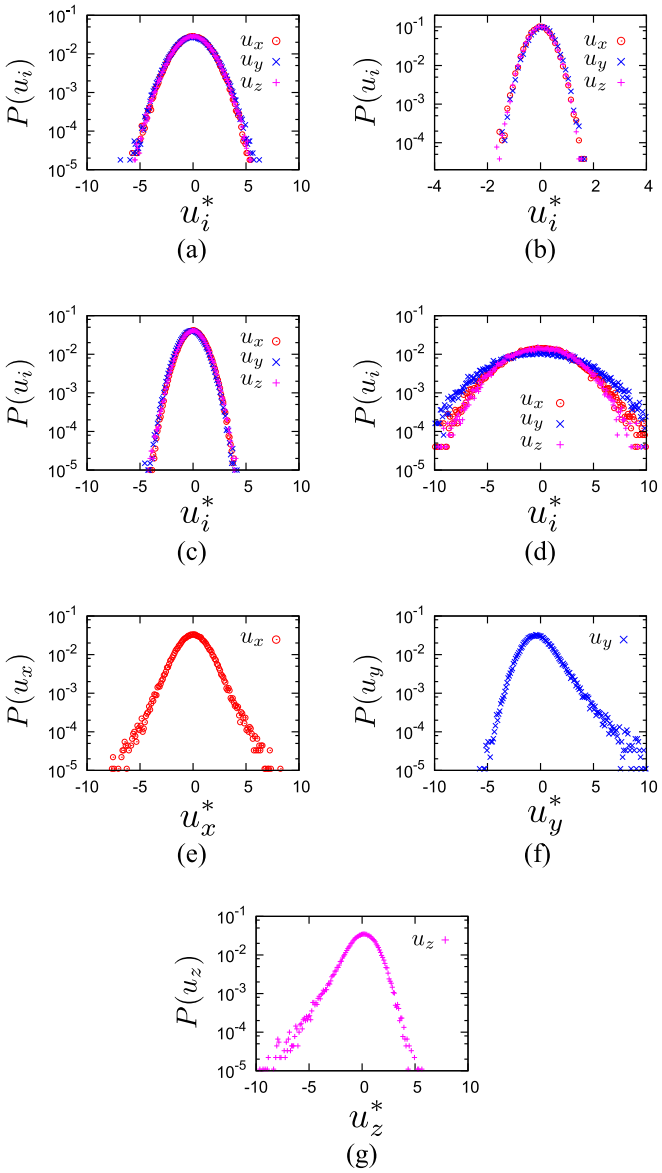

FIG. 8. (Color online) Velocity distribution functions for various phases: (a) the phase in Fig. 3(a), (b) the phase in Fig. 3(g), (c) in the dense region of the phase in Fig. 3(d), (d) in the dilute region of the phase in Fig. 3(d), (e) in the x direction at the interface of the phase in Fig. 3(d), (f) in the y direction at the interface of the phase in Fig. 3(d), and (g) in the z direction at the interface of the phase in Fig. 3(d).

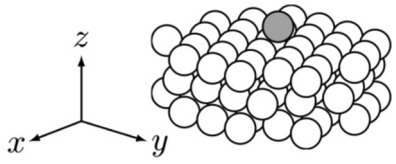

FIG. 9. Schematic picture of the configuration of a gas particle (gray) and particles in the dense region (white). We assume that the wall particles compose a face-centered-cubic lattice. We calculate the interaction energy between the gas particle and the wall particles whose distance is less than the cutoff length.

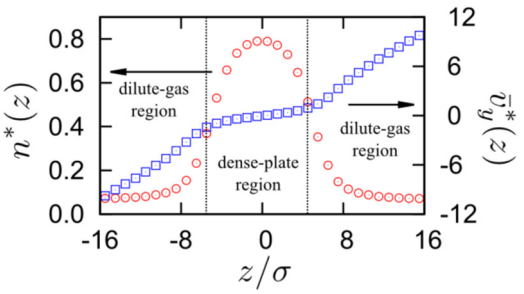

FIG. 10. (Color online) Density and velocity profiles (in the y direction) in the plate-gas coexistence phase ($n^* = 0.305$, $\dot{\gamma}^* = 10^{-0.2}$, and $\zeta^* = 10^{0.2}$), where $\bar{v}_y^*(z) = \bar{v}_y(z)\sqrt{m/\sigma\varepsilon}$.

can be converted into the Kramers equation [73–77]

$$\frac{\partial f}{\partial t} = \left\{ -\frac{\partial}{\partial \boldsymbol{r}} \cdot \left(\frac{\boldsymbol{p}}{m} + \dot{\gamma} z \hat{\boldsymbol{e}}_y \right) + \frac{\partial}{\partial \boldsymbol{p}} \cdot \left(\dot{\gamma} p_z \hat{\boldsymbol{e}}_y + \mu F_0 \frac{\boldsymbol{p}}{|\boldsymbol{p}|} + D \frac{\partial}{\partial \boldsymbol{p}} \right) \right\} f, \quad (7)$$

where $f = f(\boldsymbol{r}, \boldsymbol{p}, t)$ is the probability distribution function of the tracer particle.

If we multiply Eq. (7) by p^2 and integrate over $\boldsymbol{p}$, we immediately obtain

$$\frac{\partial}{\partial t}\langle p^2 \rangle = -\frac{\partial}{\partial \boldsymbol{r}} \cdot \frac{\langle p^2 \boldsymbol{p} \rangle}{m} - \dot{\gamma} z \frac{\partial}{\partial y}\langle p^2 \rangle - 2\dot{\gamma}\langle p_y p_z \rangle - 2\mu F_0 \langle p \rangle + 2D, \quad (8)$$

where $p = (p_y^2 + p_z^2)^{1/2}$. Because the third term on the right-hand side of Eq. (8) represents the viscous heating, which is always positive as shown in Eq. (C2), and the fourth term is the loss of the energy due to friction, the balance among the third, the fourth, and the fifth terms on right-hand side of Eq. (8) produces a steady state. It should be noted that the first and the second terms on right-hand side do not contribute to the energy balance equation for the whole system.

Here we only consider the steady distribution, i.e., $\partial f/\partial t = 0$. Thus, Eq. (7) is reduced to

$$\frac{\boldsymbol{p}}{m} \cdot \nabla f + \dot{\gamma} z \frac{\partial}{\partial y} f - \dot{\gamma} p_z \frac{\partial}{\partial p_y} f - \mu F_0 \frac{\partial}{\partial \boldsymbol{p}} \cdot \left(\frac{\boldsymbol{p}}{|\boldsymbol{p}|} f \right) - D \Delta_{\boldsymbol{p}} f = 0, \quad (9)$$

where $\Delta_{\boldsymbol{p}} = \partial^2/\partial p_y^2 + \partial^2/\partial p_z^2$. If there is neither a shear nor a density gradient, we find that Eq. (9) has the steady solution obeying an exponential distribution, i.e., $f(\boldsymbol{p}) = (\kappa^2/2\pi)\exp(-\kappa p)$, where we have introduced $\kappa \equiv \mu F_0/D$. We adopt the perturbative expression for f in terms of $\epsilon \equiv \sigma/\lambda$, which is the ratio of the diameter σ to the interface width λ, and the dimensionless shear rate $\dot{\gamma}^*$ as (see the derivation in Appendix D)

$$f(p,\theta) = f^{(0,0)}(p,\theta) + \epsilon f^{(0,1)}(p,\theta) + \dot{\gamma}^* f^{(1,0)}(p,\theta). \quad (10)$$

We also adopt the expansions

$$f^{(i,j)}(p,\theta) = \sum_{n=1}^{\infty} f_n^{(i,j)} \sin(n\theta), \tag{11}$$

with $(i,j) = (0,1)$ and $(1,0)$, where θ is the angle between $\boldsymbol{p}$ and the y axis (in the counterclockwise direction; see Fig. 7). Then we can solve Eq. (9) perturbatively as

$$f(p,\theta) = f^{(0,0)}(p) + \epsilon f_1^{(0,1)}(p)\sin\theta + \dot{\gamma}^* f_2^{(1,0)}(p)\sin 2\theta, \tag{12}$$

where $f^{(0,0)}$, $f_1^{(0,1)}$, and $f_2^{(1,0)}$ are given, respectively, by

$$f^{(0,0)}(p) = \frac{\kappa^2}{2\pi}\exp(-\kappa p), \tag{13}$$

$$f_1^{(0,1)}(p) = -\frac{A}{6\pi\kappa} p(3+\kappa p+\kappa^2 p^2)\exp(-\kappa p), \tag{14}$$

$$f_2^{(1,0)}(p) = -\frac{\kappa^2}{8\pi D t_0} p^2 \exp(-\kappa p). \tag{15}$$

Here we have introduced $t_0 = (m\sigma^2/\varepsilon)^{1/2}$ and A given by Eq. (D10). It should be noted that the other terms, except for those in Eqs. (12)–(15), automatically disappear within the linear approximation as in Eq. (10).

The second, the third, and the fourth moments in the y' and z' directions after the rotation by the angle of θ in the counterclockwise direction are given, respectively, by

$$\langle p_{y',z'}^2\rangle = \frac{3}{\kappa^2}\left(1 \mp \frac{5\dot{\gamma}}{2D\kappa^2}\sin 2(\theta-\psi)\right), \tag{16}$$

$$\langle p_{y'}^3\rangle = -\frac{765\epsilon A}{\kappa^6}\sin(\theta-\psi), \tag{17}$$

$$\langle p_{z'}^3\rangle = -\frac{765\epsilon A}{\kappa^6}\cos(\theta-\psi), \tag{18}$$

$$\langle p_{y',z'}^4\rangle = \frac{45}{\kappa^4}\left(1 \mp \frac{7\dot{\gamma}}{D\kappa^2}\sin 2(\theta-\psi)\right), \tag{19}$$

as shown in Appendix E, where $\langle p_{y',z'}^n\rangle$ with $n=2$ or 4 represents $\langle p_{y'}^n\rangle$ for a minus sign and $\langle p_{z'}^n\rangle$ for a plus sign, respectively. To reproduce the node of the third moment in the MD simulation, we phenomenologically introduce the angle ψ and replace θ by $\theta-\psi$ in Eqs. (16)–(19). Here we choose $\psi = 2\pi/9$ to fit the node position of the third moment. We have not identified the reason why the direction of the node deviates from the direction in which the VDF becomes isotropic.

Now let us compare Eqs. (16)–(19) with the MD simulation for a set of parameters $(n^*,\dot{\gamma}^*,\zeta^*) = (0.305, 10^{-0.2}, 10^{0.2})$. From the density profile (Fig. 10) and the fitting to the second moment and the amplitude of the third moment, we obtain $\epsilon \simeq 0.20$, $\mu \simeq 1.3/\sqrt{m\varepsilon}$, $D = 5.2\sqrt{m\varepsilon^3}/\sigma$, and $A \simeq 0.088/m^2\varepsilon^2$. It is surprising that Eqs. (16)–(19) can approximately reproduce the simulation results as in Fig. 11 except for the node positions of the second and the fourth moments.

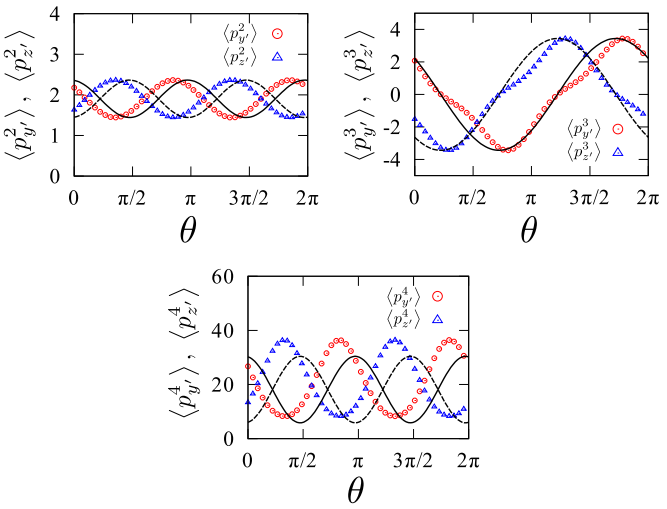

FIG. 11. (Color online) Second, third, and fourth moments obtained by MD simulations for $\rho^* = 0.305$, $\dot{\gamma}^* = 10^{-0.2}$, and $\zeta^* = 10^{0.2}$ (circles show the y' direction and triangles the z' direction) and those obtained by Eqs. (16)–(19) (the solid line shows the y' direction and the dashed line the z' direction).

For the explicit form of the VDF, we first convert $f(p,\theta)$ to $f(p_y,p_z)$ as in Appendix F:

$$f(p_y,p_z) = \frac{\kappa^2}{2\pi}\exp(-\kappa p)\Bigg(1 + \frac{\epsilon A}{3\kappa^3}(3+\kappa p+\kappa^2 p^2) \times (p_y\sin\psi - p_z\cos\psi) + \frac{\dot{\gamma}}{4D}\left[(p_y^2-p_z^2)\sin 2\psi - 2p_y p_z\cos 2\psi\right]\Bigg). \tag{20}$$

We obtain the peculiar velocity distribution function in each direction by integrating Eq. (20) with respect to u_z or u_y as

$$P(u_y) = \frac{m\kappa^2}{2\pi}\int_{-\infty}^{\infty} du_z \exp(-m\kappa u) \times \left(1 + \frac{m\epsilon A}{3\kappa^3}(3+m\kappa u+m^2\kappa^2u^2)u_y\sin\psi + \frac{m^2\dot{\gamma}}{4D}(u_y^2-u_z^2)\sin 2\psi\right), \tag{21}$$

$$P(u_z) = \frac{m\kappa^2}{2\pi}\int_{-\infty}^{\infty} du_y \exp(-m\kappa u) \times \left(1 - \frac{m\epsilon A}{3\kappa^3}(3+m\kappa u+m^2\kappa^2u^2)u_z\cos\psi + \frac{m^2\dot{\gamma}}{4D}(u_y^2-u_z^2)\sin 2\psi\right), \tag{22}$$

where $u = (u_y^2+u_z^2)^{1/2}$. These expressions semiquantitatively reproduce the VDF observed in our MD simulations as in Fig. 12.

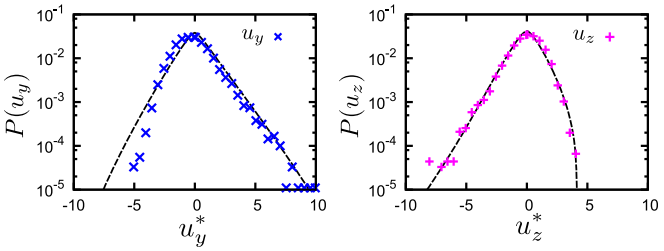

FIG. 12. (Color online) Velocity distribution functions in the y direction (crosses) and z direction (pluses) obtained by our MD simulations. The dashed lines in the left and right figures are the results of Eqs. (21) and (22), respectively.

IV. DISCUSSION

Let us discuss our results. In Sec. III A we did not discuss the time evolution of the granular temperature $T_g = (m/3N)\sum_{i=1}^{N} |\boldsymbol{v}_i - \boldsymbol{V}|^2$, where $\boldsymbol{V} = \boldsymbol{V}(\boldsymbol{r},t)$ is the ensemble average velocity field [78,79]. The granular temperature abruptly decreases to zero in the cluster phases in Figs. 3(e)–3(i) when a big cluster that absorbs all gas particles appears [65]. To clarify the mechanism of abrupt change of the temperature during clusterings, we will need to study the more detailed dynamics.

Moreover, to discuss the phase boundary between the uniformly sheared phase and the coexistence phases, we may use the stability analysis of a set of hydrodynamic equations coupled with the phase transition dynamics [80]. Once we establish the set of hydrodynamic equations, it is straightforward to perform weakly nonlinear analysis for this system [61,62,81]. It should be noted that the set of equations may be available only near the phase boundary between the uniformly sheared phase and the coexistence phases.

In Fig. 8 the VDF in a uniformly sheared phase is almost Gaussian. This result seems to be inconsistent with the results for ordinary gases under a uniform shear flow [82], which show that the VDF differs from the Gaussian function even in a uniformly sheared phase. In this study, however, we restrict our interest to only small inelastic and weakly sheared cases. This situation validates the small deviation from the Gaussian function.

V. CONCLUSION

We studied cohesive fine powders under a plane shear by controlling the density, the dimensionless shear rate, and the dissipation rate. Depending on these parameters, we found the existence of various distinct steady phases as in Fig. 3 and we have drawn the phase diagrams for several densities as in Fig. 4. In addition, the shape of clusters depends on the initial condition of velocities of particles as in Fig. 5, when the dissipation is strong. We also found that there is a quasi-particle-hole symmetry for the shape of clusters in steady states with respect to the density.

We found that the velocity distribution functions near the interface between the dense region and the gaslike dilute region in the dense-plate coexistence phase deviate from the Gaussian function as in Fig. 8. Introducing a stochastic model and its corresponding Kramers equation (7), we obtain its perturbative VDFs as in Eqs. (21) and (22), which reproduce the semiquantitative behavior of the VDF observed in MD simulations as in Fig. 12. This result suggests that the motion of a gas particle near the interface is subjected to Coulombic friction force whose origin is the activation energy in the dense region.

ACKNOWLEDGMENTS

The authors thank Takahiro Hatano and Meheboob Alam for their fruitful advice. K.S. wishes to express his sincere gratitude to the Yukawa Institute for Theoretical Physics (YITP) for support for his stay and its warm hospitality. Part of this work was performed during the YITP workshops No. YITP-W-13-04 on "Physics of Glassy and Granular Materials" and No. YITP-T-13-03 on "Physics of Granular Flow." Numerical computation in this work was partially carried out at the Yukawa Institute Computer Facility. This work was partially supported by JSPS KAKENHI Grant No. 25287098.

APPENDIX A: RESULTS OF THE PHYSICAL BOUNDARY CONDITION

In this appendix we present the results of our simulations under the flat boundary condition, which is one of the typical physical boundaries to clarify the influence of the boundary condition. We prepare flat walls at $z = \pm L/2$, moving at velocities $\pm\dot{\gamma}L/2$ in the y direction, respectively. When a particle with a velocity (v_x, v_y, v_z) hits the walls at $z = \pm L/2$, the velocity changes as $(v_x, \pm\dot{\gamma}L/2 - v_y, -v_z)$ after the collision, respectively. The phase diagram of the system for the physical boundary for $n^* = 0.305$ is presented in Fig. 13. We have obtained three steady phases: the uniformly sheared phase, the coexistence phase between the dense-plate and gas regions, and the dense-plate cluster phase. The phase diagram is almost the same as the corresponding one under the Lees-Edwards boundary condition [see Fig. 4(d)]. This can be understood as follows: If two particles at the symmetric positions with respect to the origin of the system simultaneously collide with the walls at $z = L/2$ and $-L/2$, the pair of velocities after collisions is the same as that after passing across the boundaries at $z = \pm L/2$ for the system under the Lees-Edwards boundary condition. This

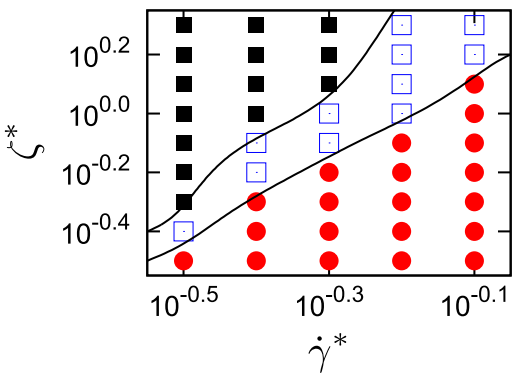

FIG. 13. (Color online) Phase diagram under the flat boundary condition for $n^* = 0.305$: a uniformly sheared state [red solid circles, Fig. 3(a)], the coexistence of a dense plate and gases [blue open squares, Fig. 3(d)], and an isolated dense plate [black solid squares, Fig. 3(g)].

is realized after the averaging over the collisions. Thus, the flat boundary condition is essentially equivalent to the Lees-Edwards boundary condition.

APPENDIX B: CALCULATION OF THE COULOMBIC FRICTION CONSTANT

In this appendix we try to illustrate the existence of the Coulombic friction force for the motion of a tracer particle near the interface. Let us consider a situation that a gas particle hits and slides on the wall formed by the particles in the dense region (see Fig. 9). If the kinetic energy of the gas particle is less than the potential energy formed by the particles in the dense region, it should be trapped in the potential well. Therefore, the motion of the gas particle is restricted near the interface. In this case, we can write the N-body distribution function near the interface $\rho(\mathbf{\Gamma},t)$ by using the distribution function in the equilibrium system as [67,83–85]

$$\rho(\mathbf{\Gamma},t)=\rho_{\rm eq}(\mathbf{\Gamma})\exp\left(\int_0^t d\tau\,\Omega(-\tau,\mathbf{\Gamma},\dot\gamma_l,\zeta)\right), \tag{B1}$$

where $\mathbf{\Gamma}=\{\boldsymbol{r}_i,\boldsymbol{p}_i\}_{i=1}^N$, $\rho_{\rm eq}(\mathbf{\Gamma})$ is the equilibrium distribution function at time $t=0$, and

$$\begin{aligned}\Omega(t,\mathbf{\Gamma},\dot\gamma,\zeta)=&-\beta\dot\gamma V\sigma_{yz}(t,\mathbf{\Gamma},\dot\gamma,\zeta)\\&-2\beta\mathcal{R}(t,\mathbf{\Gamma},\dot\gamma,\zeta)-\Lambda(t,\mathbf{\Gamma},\dot\gamma,\zeta),\end{aligned} \tag{B2}$$

with

$$\begin{aligned}\sigma_{\alpha\beta}(t,\mathbf{\Gamma},\dot\gamma,\zeta)=&\sum_i\left\{\frac{p_{i,\alpha}p_{i,\beta}}{m}-\sum_{j\neq i}r_{i,\alpha}\frac{\partial U^{\rm LJ}(r_{ij})}{\partial r_{i,\beta}}\right.\\&\left.+\sum_{j\neq i}r_{i,\alpha}F_\beta^{\rm vis}(\boldsymbol{r}_{ij},\boldsymbol{v}_{ij})\right\},\end{aligned} \tag{B3}$$

$$\mathcal{R}(t,\mathbf{\Gamma},\dot\gamma,\zeta)=\frac{\zeta}{4}\sum_{i\neq j}\Theta(\sigma-r_{ij})(\boldsymbol{v}_{ij}\cdot\hat{\boldsymbol{r}}_{ij})^2, \tag{B4}$$

$$\Lambda(t,\mathbf{\Gamma},\dot\gamma,\zeta)=-\frac{\zeta}{m}\sum_{i\neq j}\Theta(\sigma-r_{ij}), \tag{B5}$$

$$F_\beta^{\rm vis}(\boldsymbol{r}_{ij},\boldsymbol{v}_{ij})=-\zeta\Theta(\sigma-r_{ij})(\boldsymbol{v}_{ij}\cdot\hat{\boldsymbol{r}}_{ij})\frac{r_{ij,\beta}}{r_{ij}}. \tag{B6}$$

Here we have introduced the inverse granular temperature $\beta=1/T$ and the local shear rate $\dot\gamma_l$ in the interface region. If the dissipation is small and the shear rate is not large, we may assume that $\Omega(-t)\simeq-\beta\dot\gamma V\sigma_{yz}^{\rm MF}(-t)$, where $\sigma_{yz}^{\rm MF}$ is the mean-field yz component of the stress tensor. We also assume that the stress tensor decays exponentially as $\sigma_{yz}^{\rm MF}(-t)\simeq\sigma_{yz}^{\rm MF}(0)\exp(-|t|/\tau_0)$ [67], where τ_0 is the relaxation time of the stress tensor. From these relationships we may use the approximate expression

$$\begin{aligned}\rho(\mathbf{\Gamma},t)\simeq&\prod_{i=1}^{N_l}\frac{1}{Z^{\rm MF}}\exp[-\beta(H^{\rm MF}-\Delta E_i)]\\&\times\exp\left[-\beta\tau_0\dot\gamma_l V_l\sigma_{yz}^{\rm MF}(0)\right],\end{aligned} \tag{B7}$$

where $H^{\rm MF}$ and ΔE_i are, respectively, the mean-field Hamiltonian per particle in the interface and the energy fluctuation of the particle i, which may be the activation energy from the local trap. Here N_l and V_l are, respectively, the number of particles and the volume in the interface region and $Z^{\rm MF}=\int d\boldsymbol{r}\,d\boldsymbol{p}\exp(-\beta H^{\rm MF})$. There are two characteristic time scales $\dot\gamma^{-1}$ and $\dot\gamma_l^{-1}$ corresponding to the uniform region and the interface between dense and dilute regions. Because the time scale is obtained from the average over the distribution function (B7) or the local mean-field distribution, the relationship between $\dot\gamma^{-1}$ and $\dot\gamma_l^{-1}$ is expected to be

$$\dot\gamma_l^{-1}=\dot\gamma^{-1}\exp\left\{\beta\left[\Delta E-\tau_0\dot\gamma_l V_l\sigma_{yz}^{\rm MF}(0)\right]\right\}, \tag{B8}$$

where we have eliminated the subscript i for the particle. This equation can be rewritten as

$$\sigma_{yz}^{\rm MF}(0)=\frac{1}{\tau_0\dot\gamma_l V_l}\left(\Delta E+T\ln\frac{\dot\gamma_l}{\dot\gamma}\right). \tag{B9}$$

Therefore, we may estimate Coulombic friction constant as

$$\mu=\frac{\sigma_{yz}^{\rm MF}(0)}{P}=\frac{1}{\tau_0\dot\gamma_l PV_l}\left(\Delta E+T\ln\frac{\dot\gamma_l}{\dot\gamma}\right), \tag{B10}$$

where $P\simeq0.90\varepsilon/\sigma^3$, $V_l\simeq4.3\sigma^3$, $\Delta E\simeq3.5\varepsilon$, and $\dot\gamma_l\simeq0.83(\varepsilon/m\sigma^2)^{1/2}$ at the interface for a set of parameters $(n^*,\dot\gamma^*,\zeta^*)=(0.305,10^{-0.2},10^{0.2})$. In this expression we cannot determine the relaxation time τ_0 from the simulation, which is estimated to reproduce the average value of the second moment with the aid of Eq. (16).

APPENDIX C: DETAILED CALCULATION OF THE VISCOUS HEATING TERM

In this appendix let us calculate the average of the viscous heating term by using the distribution function near the interface. From Eq. (B7) we can rewrite the distribution function with the aid of Eq. (B3) as

$$\rho(\mathbf{\Gamma},t)\approx\frac{1}{Z}\prod_{i=1}^{N_l}\exp\left[-\beta\left(\frac{\boldsymbol{p}_i^2}{2m}+\tau_0\dot\gamma_l V_l\frac{p_{i,y}p_{i,z}}{m}\right)\right], \tag{C1}$$

where $Z=\int\prod_{i=1}^{N_l}d\boldsymbol{r}_i d\boldsymbol{p}_i\exp[-\beta(\boldsymbol{p}_i^2/2m+\tau_0\dot\gamma_l V_l p_{i,y}p_{i,z}/m)]$. Then $\langle p_y p_z\rangle$ is given by

$$\begin{aligned}\langle p_y p_z\rangle=&\int d\mathbf{\Gamma}\,p_{i,y}p_{i,z}\rho(\mathbf{\Gamma},t)\\\propto&\int_{-\infty}^{\infty}dp_{i,y}\int_{-\infty}^{\infty}dp_{i,z}p_{i,y}p_{i,z}\\&\times\exp\left[-\beta\left(\frac{\boldsymbol{p}_i^2}{2m}+\tau_0\dot\gamma_l V_l\frac{p_{i,y}p_{i,z}}{m}\right)\right]\\=&\int_0^\infty dp\int_0^{2\pi}d\theta p^3\sin\theta\cos\theta\\&\times\exp\left[-\beta\left(\frac{p^2}{2m}+\frac{\tau_0\dot\gamma_l V_l}{m}p^2\sin\theta\cos\theta\right)\right]\\=&-\frac{\pi}{2}\int_0^\infty dp\,p^3\exp\left(-\frac{\beta p^2}{2m}\right)I_1\left(\frac{\beta\tau_0\dot\gamma_l V_l}{2m}p^2\right),\end{aligned} \tag{C2}$$

where $I_1(x)$ is the modified Bessel function of the first kind [86]. Because $I_1(x)$ is positive for $x>0$, Eq. (C2) ensures that

the viscous heating term $-\dot{\gamma}\langle p_y p_z\rangle$ is always positive near the interface.

APPENDIX D: PERTURBATION SOLUTION OF THE KRAMERS EQUATION

In this appendix let us solve the Kramers equation (9) perturbatively to obtain the steady VDF. Later we compare this solution with the result of MD simulations.

First, we adopt the following three assumptions. The first assumption is that the distribution function is independent of both x and y, the coordinates horizontal to the interface. We also assume that the distribution function f depends on z, vertical to the interface, through the density and the granular temperature:

$$\frac{\partial f}{\partial z}=\frac{\partial f}{\partial n}\frac{dn}{dz}+\frac{\partial f}{\partial T}\frac{dT}{dz}. \tag{D1}$$

Second, we assume that the changes of the density and the granular temperature near the interface can be characterized by the interface width λ as

$$\frac{dn}{dz}\simeq-\frac{n_0}{\lambda},\quad \frac{dT}{dz}\simeq\frac{T_0}{\lambda}, \tag{D2}$$

where $n_0=n(z_0)=(n_l+n_g)/2$ and $T_0=T(z_0)=(T_l+T_g)/2$. Here n_l and T_l are the density and the granular temperature in the dense region and n_g and T_g are those in the dilute region, respectively. Third, we also assume that the interface width λ is much longer than the diameter of the particles σ, i.e., $\epsilon\equiv\sigma/\lambda\ll 1$. From these assumptions $\partial f/\partial z$ may be rewritten as

$$\frac{\partial f}{\partial z}\simeq-\epsilon\left(\frac{n_0}{\sigma}\frac{\partial}{\partial n}-\frac{T_0}{\sigma}\frac{\partial}{\partial T}\right)f. \tag{D3}$$

To solve Eq. (9) we adopt the perturbative expression (10). Equation (9) thus reduces to the following three equations: For the zeroth order,

$$-\kappa\frac{\partial}{\partial \boldsymbol{p}}\cdot\left(\frac{\boldsymbol{p}}{|\boldsymbol{p}|}f^{(0,0)}\right)-\Delta_{\boldsymbol{p}}f^{(0,0)}=0; \tag{D4}$$

for the first order of ϵ,

$$-\frac{p_z}{mD}\left(\frac{n_0}{\sigma}\frac{\partial}{\partial n}-\frac{T_0}{\sigma}\frac{\partial}{\partial T}\right)f^{(0,0)}-\kappa\frac{\partial}{\partial \boldsymbol{p}}\cdot\left(\frac{\boldsymbol{p}}{|\boldsymbol{p}|}f^{(0,1)}\right)-\Delta_{\boldsymbol{p}}f^{(0,1)}=0; \tag{D5}$$

and for the first order of $\dot{\gamma}^*$,

$$-\frac{p_z}{D}\frac{\partial f^{(0,0)}}{\partial p_y}-\kappa\frac{\partial}{\partial \boldsymbol{p}}\cdot\left(\frac{\boldsymbol{p}}{|\boldsymbol{p}|}f^{(1,0)}\right)-\Delta_{\boldsymbol{p}}f^{(1,0)}=0. \tag{D6}$$

The solution of Eq. (D4) is given by

$$f^{(0,0)}=C_1\exp(-\kappa p)+C_2\exp(-\kappa p)\mathrm{Ei}(\kappa p), \tag{D7}$$

where $\mathrm{Ei}(x)$ is the exponential integral $\mathrm{Ei}(x)\equiv-\int_{-x}^{\infty}(e^{-t}/t)dt$ [86] and C_1 and C_2 are the normalization constants. Here we set $C_2=0$ because $\mathrm{Ei}(x)$ becomes infinite at $x=0$ and $C_1=\kappa^2/2\pi$ to satisfy the normalization condition without the shear and the density gradient. Using Eq. (D7), Eqs. (D5) and (D6) can be represented in polar coordinates as

$$A\left(p^2-\frac{2}{\lambda}p\right)f^{(0,0)}\sin\theta=\kappa\left(\frac{1}{p}+\frac{\partial}{\partial p}\right)f^{(0,1)}+\left(\frac{\partial^2}{\partial p^2}+\frac{1}{p}\frac{\partial}{\partial p}+\frac{1}{p^2}\frac{\partial^2}{\partial\theta^2}\right)f^{(0,1)} \tag{D8}$$

and

$$\frac{\kappa}{2Dt_0}pf^{(0,0)}\sin 2\theta=\kappa\left(\frac{1}{p}+\frac{\partial}{\partial p}\right)f^{(1,0)}+\left(\frac{\partial^2}{\partial p^2}+\frac{1}{p}\frac{\partial}{\partial p}+\frac{1}{p^2}\frac{\partial^2}{\partial\theta^2}\right)f^{(1,0)}, \tag{D9}$$

where we have introduced A as

$$A=\frac{n_0}{m\sigma D}\frac{\partial\kappa}{\partial n}-\frac{T_0}{m\sigma D}\frac{\partial\kappa}{\partial T}. \tag{D10}$$

To solve Eqs. (D8) and (D9) we adopt the expansions for $f^{(i,j)}(p,\theta)=\sum_{n=1}^{\infty}f_n^{(i,j)}(p)\sin(n\theta)$ with $(i,j)=(0,1)$ and $(1,0)$ [77]. Equation (D8) for each n reduces to the following equations: For $n=1$,

$$\frac{A\kappa^2}{2\pi}\left(p^2-\frac{2}{\kappa}p\right)\exp(-\kappa p)=\kappa\left(\frac{1}{p}+\frac{\partial}{\partial p}\right)f_1^{(0,1)}+\left(\frac{\partial^2}{\partial p^2}+\frac{1}{p}\frac{\partial}{\partial p}-\frac{1}{p^2}\right)f_1^{(0,1)}, \tag{D11}$$

and for $n\neq 1$,

$$0=\kappa\left(\frac{1}{p}+\frac{\partial}{\partial p}\right)f_n^{(0,1)}+\left(\frac{\partial^2}{\partial p^2}+\frac{1}{p}\frac{\partial}{\partial p}-\frac{n^2}{p^2}\right)f_n^{(0,1)}. \tag{D12}$$

The solutions of Eqs. (D11) and (D12) are given, respectively, by

$$f_1^{(0,1)}=\frac{C_{11}}{p}+C_{12}\frac{1+\kappa p}{\kappa^2 p}-\frac{A}{6\pi}\frac{6+6\kappa p+3\kappa^2p^2+\kappa^3p^3+\kappa^4p^4}{\kappa^3 p}\exp(-\kappa p) \tag{D13}$$

and

$$f_n^{(0,1)}=C_{n1}(\kappa p)^n\exp(-\kappa p)U(n,2n+1,\kappa p)+C_{n2}(\kappa p)^n\exp(-\kappa p)L_{-n}^{2n}(\kappa p) \tag{D14}$$

for $n\neq 1$, where $U(a,b,x)$ and $L_a^b(x)$ are, respectively, the confluent hypergeometric function and Laguerre's bipolynomial [86] and the normalization constants C_{n1} and C_{n2} $(n=1,2,\ldots)$ will be determined later. Similarly, Eq. (D9) for each n reduces to the following equations: For $n=2$,

$$\frac{\kappa^3}{4\pi Dt_0}p\exp(-\kappa p)=\kappa\left(\frac{1}{p}+\frac{\partial}{\partial p}\right)f_2^{(1,0)}+\left(\frac{\partial^2}{\partial p^2}+\frac{1}{p}\frac{\partial}{\partial p}-\frac{4}{p^2}\right)f_2^{(1,0)}, \tag{D15}$$

and for $n \neq 2$,

$$0 = \kappa \left(\frac{1}{p} + \frac{\partial}{\partial p} \right) f_n^{(1,0)} + \left(\frac{\partial^2}{\partial p^2} + \frac{1}{p} \frac{\partial}{\partial p} - \frac{n^2}{p^2} \right) f_n^{(1,0)}. \tag{D16}$$

The solutions of Eqs. (D15) and (D16) are given, respectively, by

$$f_2^{(1,0)} = C_{23} \frac{3 - \kappa p}{p^2} + C_{24} \frac{6 + 4\kappa p + \kappa^2 p^2}{\kappa^4 p^2} \exp(-\kappa p) + \frac{1}{8\pi D t_0} \frac{72 + 48\kappa p + 12\kappa^2 p^2 - \kappa^4 p^4}{\kappa^2 p^2} \exp(-\kappa p) \tag{D17}$$

and

$$f_n^{(1,0)} = C_{n3} (\kappa p)^n \exp(-\kappa p) U(n, 2n+1, \kappa p) + C_{n4} (\kappa p)^n \exp(-\kappa p) L_{-n}^{2n}(\kappa p) \tag{D18}$$

for $n \neq 2$, where the normalization constants C_{n3} and C_{n4} ($n = 1,2,\ldots$) will be determined later.

Here let us determine the normalization constants $C_{n1}, \ldots, C_{n4}$ ($n = 1,2,\ldots$). The distributions $f_n^{(0,1)}$ and $f_n^{(1,0)}$ should be finite at $p = 0$ and approach zero for large p. Therefore, we obtain

$$\begin{aligned} &C_{11} = 0, \quad C_{12} = \frac{A}{\pi\kappa}, \quad C_{23} = 0, \quad C_{24} = -\frac{3\kappa^2}{2\pi D t_0}, \\ &C_{n1} = 0, \quad C_{n2} = 0 \quad (n \neq 1), \\ &C_{n3} = 0, \quad C_{n4} = 0 \quad (n \neq 2). \end{aligned} \tag{D19}$$

From these results we obtain

$$f(p,\theta) = f^{(0,0)} + \epsilon f_1^{(0,1)} \sin\theta + \dot{\gamma}^* f_2^{(1,0)} \sin 2\theta, \tag{D20}$$

where $f^{(0,0)}$, $f_1^{(0,1)}$, and $f_2^{(1,0)}$ are given, respectively, by

$$f^{(0,0)}(p) = \frac{\kappa^2}{2\pi} \exp(-\kappa p), \tag{D21}$$

$$f_1^{(0,1)}(p) = -\frac{A}{6\pi\kappa} p(3 + \kappa p + \kappa^2 p^2) \exp(-\kappa p), \tag{D22}$$

$$f_2^{(1,0)}(p) = -\frac{\kappa^2}{8\pi D t_0} p^2 \exp(-\kappa p). \tag{D23}$$

APPENDIX E: DETAILED CALCULATIONS OF VARIOUS MOMENTS

In this appendix we calculate the nth moments of $p_{y'}$ and $p_{z'}$ using the distribution function obtained in Appendix D. From the definition of the moment, the nth moment of an arbitrary function $G(\boldsymbol{p})$ is given by

$$\langle G^n \rangle = \int d\boldsymbol{p}\, G^n(p,\varphi) f(p,\varphi). \tag{E1}$$

We rotate the coordinate the coordinate (y,z) by θ counterclockwise and introduce the new Cartesian coordinate (y',z') as in Fig. 7. From this definition we obtain the nth moments of $p_{y'}$: For $n = 2$,

$$\begin{aligned} \langle p_{y'}^2 \rangle &= \int_0^\infty dp \int_0^{2\pi} d\varphi p^3 \cos^2(\varphi - \theta) \\ &\quad \times \left[f^{(0,0)}(p) + \epsilon f_1^{(0,1)}(p) \sin\varphi + \dot{\gamma}^* f_2^{(1,0)}(p) \sin 2\varphi \right] \\ &= \frac{3}{\kappa^2} \left(1 - \frac{5\dot{\gamma}}{2D\kappa^2} \sin 2\theta \right); \end{aligned} \tag{E2}$$

for $n = 3$,

$$\begin{aligned} \langle p_{y'}^3 \rangle &= \int_0^\infty dp \int_0^{2\pi} d\varphi p^4 \cos^3(\varphi - \theta) \\ &\quad \times \left[f^{(0,0)}(p) + \epsilon f_1^{(0,1)}(p) \sin\varphi + \dot{\gamma}^* f_2^{(1,0)}(p) \sin 2\varphi \right] \\ &= -\frac{765\epsilon A}{\kappa^7} \sin\theta; \end{aligned} \tag{E3}$$

and for $n = 4$,

$$\begin{aligned} \langle p_{y'}^4 \rangle &= \int_0^\infty dp \int_0^{2\pi} d\varphi p^5 \cos^4(\varphi - \theta) \\ &\quad \times \left[f^{(0,0)}(p) + \epsilon f_1^{(0,1)}(p) \sin\varphi + \dot{\gamma}^* f_2^{(1,0)}(p) \sin 2\varphi \right] \\ &= \frac{45}{\kappa^4} \left(1 - \frac{7\dot{\gamma}}{D\kappa^2} \sin 2\theta \right). \end{aligned} \tag{E4}$$

Similarly, we can calculate the each moment of $p_{z'}$ so that we obtain Eqs. (16)–(19).

APPENDIX F: VELOCITY DISTRIBUTION FUNCTION FOR EACH DIRECTION

In this appendix we derive the velocity distribution function in the Cartesian coordinate (y,z) and calculate the velocity distribution functions in the y and z directions. The velocity distribution function in polar coordinates (p,θ) is given by Eq. (12), where we replace θ by $\theta - \psi$ as in Eqs. (16)–(19), which can be converted into the form of the Cartesian coordinate as

$$\begin{aligned} f(p_y, p_z) &= \frac{\kappa^2}{2\pi} \exp(-\kappa p) \left(1 - \frac{\epsilon A}{3\kappa^3} p(3 + \kappa p + \kappa^2 p^2) \right. \\ &\quad \left. \times \sin(\theta - \psi) - \frac{\dot{\gamma}}{4D} p^2 \sin 2(\theta - \psi) \right) \\ &= \frac{\kappa^2}{2\pi} \exp(-\kappa p) \left(1 + \frac{\epsilon A}{3\kappa^3} (3 + \kappa p + \kappa^2 p^2) \right. \\ &\quad \times (p_y \sin\psi - p_z \cos\psi) \\ &\quad \left. + \frac{\dot{\gamma}}{4D} \left[\left(p_y^2 - p_z^2 \right) \sin 2\psi - 2 p_y p_z \cos 2\psi \right] \right), \end{aligned} \tag{F1}$$

where $p = \sqrt{p_y^2 + p_z^2}$. Next let us calculate the velocity distribution functions in the y and z directions. In this paper we focus on the VDF for the fluctuation velocity, which is defined by the deviation from the average velocity. Therefore, we can replace p_y and p_z by mu_y and mu_z in Eq. (F1). The

velocity distribution function in the y direction $P(u_y)$ is given by integrating Eq. (F1) with respect to u_z as

$$P(u_y) = \int_{-\infty}^{\infty} d(mu_z) f(mu_y, mu_z)$$
$$= \frac{m\kappa^2}{2\pi} \int_{-\infty}^{\infty} du_z \exp(-m\kappa u) \Bigg(1 + \frac{m\epsilon A}{3\kappa^3} (3 + m\kappa u + m^2\kappa^2 u^2) u_y \sin\psi + \frac{m^2\dot{\gamma}}{4D} (u_y^2 - u_z^2) \sin 2\psi \Bigg), \tag{F2}$$

where $u = \sqrt{u_y^2 + u_z^2}$. Similarly, we can calculate the velocity distribution function in the z direction $P(p_z)$ as

$$P(u_z) = \int_{-\infty}^{\infty} d(mu_y) f(mu_y, mu_z)$$
$$= \frac{m\kappa^2}{2\pi} \int_{-\infty}^{\infty} du_y \exp(-m\kappa u) \Bigg(1 - \frac{m\epsilon A}{3\kappa^3} (3 + m\kappa u + m^2\kappa^2 u^2) u_z \cos\psi + \frac{m^2\dot{\gamma}}{4D} (u_y^2 - u_z^2) \sin 2\psi \Bigg). \tag{F3}$$

[1] H. Krupp, Adv. Colloid Interface Sci. **1**, 111 (1967).
[2] J. Visser, Powder Technol. **58**, 1 (1989).
[3] J. M. Valverde, A. Castellanos, A. Ramos, and P. K. Watson, Phys. Rev. E **62**, 6851 (2000).
[4] J. Tomas, Particul. Sci. Technol. **19**, 95 (2001).
[5] F. Cansell, C. Aymonier, and A. Loppinet-Serani, Curr. Opin. Solid State Mater. Sci. **7**, 331 (2003).
[6] J. Tomas, Granul. Matter **6**, 75 (2004).
[7] A. Castellanos, Adv. Phys. **54**, 263 (2005).
[8] H.-J. Butt, B. Cappella, and M. Kappl, Surf. Sci. Rep. **59**, 1 (2005).
[9] J. Tomas, Chem. Eng. Sci. **62**, 1997 (2007).
[10] R. Tykhoniuk, J. Tomas, S. Luding, M. Kappl, L. Heim, and H.-J. Butt, Chem. Eng. Sci. **62**, 2843 (2007).
[11] G. Calvert, M. Ghadiri, and R. Tweedie, Adv. Powder Technol. **20**, 4 (2009).
[12] J. R. van Ommen, J. M. Valverde, and R. Pfeffer, J. Nanopart. Res. **14**, 1 (2012).
[13] J. N. Israelachvili, *Intermolecular and Surface Forces*, 3rd ed. (Academic, New York, 2011).
[14] K. L. Johnson, K. Kendall, and A. D. Roberts, Proc. R. Soc. London Ser. A **324**, 301 (1971).
[15] B. V. Derjaguin, I. I. Abrikosova, and E. M. Lifshitz, Chem. Soc. Rev. **10**, 295 (1956).
[16] B. V. Derjaguin, V. M. Muller, and Y. P. Toporov, J. Colloid Interface Sci. **53**, 314 (1975).
[17] K. Z. Y. Yen and T. K. Chaki, J. Appl. Phys. **71**, 3164 (1992).
[18] C. Thornton, K. K. Yin, and M. J. Adams, J. Phys. D **29**, 424 (1996).
[19] T. Mikami, H. Kamiya, and M. Horio, Chem. Eng. Sci. **53**, 1927 (1998).
[20] G. Bartels, T. Unger, D. Kadau, D. E. Wolf, and J. Kertész, Granul. Matter **7**, 139 (2005).
[21] S. Luding, R. Tukhoniuk, and J. Tomas, Chem. Eng. Technol. **26**, 1229 (2003).
[22] S. Luding, Powder Technol. **158**, 45 (2005).
[23] S. Luding, Granul. Matter **10**, 235 (2008).
[24] J. R. Royer, D. J. Evans, L. Oyarte, E. Kapit, M. Möbius, S. R. Waitukatis, and H. M. Jaeger, Nature (London) **459**, 1110 (2009).
[25] N. Kumar and S. Luding, arXiv:1407.6167.
[26] S. Gonzalez, A. R. Thornton, and S. Luding, Eur. Phys. J. Special Topics **223**, 2205 (2014).
[27] D. Hornbaker, R. Albert, I. Albert, A.-L. Barabási, and P. Schiffer, Nature (London) **387**, 765 (1997).
[28] L. Bocquet, E. Charlaix, S. Ciliberto, and J. Crassous, Nature (London) **396**, 735 (1998).
[29] C. D. Willett, M. J. Adams, S. A. Johnson, and J. P. K. Seville, Langmuir **16**, 9396 (2000).
[30] S. T. Nase, W. L. Vargas, A. A. Abatan, and J. J. MacCarthy, Powder Technol. **116**, 214 (2001).
[31] S. Herminghaus, Adv. Phys. **54**, 221 (2005).
[32] N. Mitarai and F. Nori, Adv. Phys. **55**, 1 (2006).
[33] S. Ulrich and A. Zippelius, Phys. Rev. Lett. **109**, 166001 (2012).
[34] F. Gerl and A. Zippelius, Phys. Rev. E **59**, 2361 (1999).
[35] H. Hayakawa and H. Kuninaka, Chem. Eng. Sci. **57**, 239 (2002).
[36] A. Awasthi, S. C. Hendy, P. Zoontjens, and S. A. Brown, Phys. Rev. Lett. **97**, 186103 (2006).
[37] N. V. Brilliantov, N. Albers, F. Spahn, and T. Pöschel, Phys. Rev. E **76**, 051302 (2007).
[38] M. Suri and T. Dumitrică, Phys. Rev. B **78**, 081405 (2008).
[39] H. Kuninaka and H. Hayakawa, Phys. Rev. E **79**, 031309 (2009).
[40] K. Saitoh, A. Bodrova, H. Hayakawa, and N. V. Brilliantov, Phys. Rev. Lett. **105**, 238001 (2010).
[41] H. Kuninaka and H. Hayakawa, Phys. Rev. E **86**, 051302 (2012).
[42] H. Tanaka, K. Wada, T. Suyama, and S. Okuzumi, Prog. Theor. Phys. Supp. **195**, 101 (2012).
[43] R. Murakami and H. Hayakawa, Phys. Rev. E **89**, 012205 (2014).
[44] J.-P. Hansen and L. Verlet, Phys. Rev. **184**, 151 (1969).
[45] J. J. Nicolas, K. E. Gubbins, W. B. Streett, and D. J. Tildersley, Mol. Phys. **37**, 1429 (1979).
[46] Y. Adachi, I. Fijihara, M. Takamiya, and K. Nakanishi, Fluid Phase Equilibr. **39**, 1 (1988).
[47] A. Lotfi, J. Vrabec, and J. Fischer, Mol. Phys. **76**, 1319 (1992).
[48] J. K. Johnson, J. A. Zollweg, and K. E. Gubbins, Mol. Phys. **78**, 591 (1993).
[49] J. Kolafa, H. L. Vörtler, K. Aim, and I. Nezbeda, Mol. Simulat. **11**, 305 (1993).
[50] R. H. Heist and H. He, J. Phys. Chem. Ref. Data **23**, 781 (1994).
[51] A. Laaksonen and D. Kashchiev, J. Chem. Phys. **98**, 7748 (1994).
[52] K. Yasuoka and M. Matsumoto, J. Chem. Phys. **109**, 8451 (1998).
[53] I. Goldhirsch and G. Zanetti, Phys. Rev. Lett. **70**, 1619 (1993).
[54] I. Goldhirsch, M.-L. Tan, and G. Zanetti, J. Sci. Comput. **8**, 1 (1993).

[55] S. McNamara and W. R. Young, Phys. Rev. E **53**, 5089 (1996).
[56] S. McNamara, Phys. Fluids A **5**, 3056 (1993).
[57] N. Brilliantov, C. Salueña, T. Schwager, and T. Pöschel, Phys. Rev. Lett. **93**, 134301 (2004).
[58] M. E. Lasinski, J. S. Curtis, and J. F. Pekny, Phys. Fluids **16**, 265 (2004).
[59] S. L. Conway and B. J. Glasser, Phys. Fluids **16**, 509 (2004).
[60] K. Saitoh and H. Hayakawa, Phys. Rev. E **75**, 021302 (2007).
[61] M. Alam and P. Shukla, J. Fluid Mech. **716**, 349 (2013).
[62] P. Shukla and M. Alam, J. Fluid Mech. **718**, 131 (2013).
[63] Y. Gu, S. Chialvo, and S. Sundaresan, Phys. Rev. E **90**, 032206 (2014).
[64] A. W. Lees and S. F. Edwards, J. Phys. C **5**, 1921 (1972).
[65] S. Takada and H. Hayakawa, in *Powders and Grains 2013, Proceedings of the Seventh International Conference on Micromechanics of Granular Media*, edited by A. Yu, K. Dong, R. Yang, and S. Luding, AIP Conf. Proc. No. 1542 (AIP, New York, 2013), p. 819.
[66] D. J. Evans and G. P. Morriss, Phys. Rev. A **30**, 1528 (1984).
[67] D. J. Evans and G. Morriss, *Statistical Mechanics of Nonequilibrium Liquids*, 2nd ed. (Cambridge University Press, Cambridge, 2008).
[68] D. Chandler and J. D. Weeks, Phys. Rev. Lett. **25**, 149 (1970).
[69] J. D. Weeks, D. Chandler, and H. C. Andersen, J. Chem. Phys. **54**, 5237 (1971).
[70] S. Takada and H. Hayakawa, in *Proceedings of the Fourth International Symposium on Slow Dynamics in Complex Systems: Keep Going Tohoku*, edited by M. Tokuyama and I. Oppenheim, AIP Conf. Proc. No. 1518 (AIP, New York, 2013), p. 741.
[71] K. C. Vijayakumar and M. Alam, Phys. Rev. E **75**, 051306 (2007).
[72] M. Alam and V. K. Chikkadi, J. Fluid Mech. **653**, 175 (2010).
[73] R. Kubo, M. Toda, and N. Hashitsume, *Statistical Physics II: Nonequilibrium Statistical Mechanics* (Springer, Berlin, 1991).
[74] R. Zwanzig, *Nonequilibrium Statistical Mechanics* (Oxford University Press, New York, 2001).
[75] A. Kawarada and H. Hayakawa, J. Phys. Soc. Jpn. **73**, 2037 (2004).
[76] P.-G. de Gennes, J. Stat. Phys. **119**, 953 (2005).
[77] H. Hayakawa, Physica D **205**, 48 (2005).
[78] I. Goldhirsch, Annu. Rev. Fluid Mech. **35**, 267 (2003).
[79] I. Goldhirsch, Powder Technol. **182**, 130 (2008).
[80] A. Onuki, *Phase Transition Dynamics* (Cambridge University Press, Cambridge, 2002).
[81] K. Saitoh and H. Hayakawa, Granul. Matter **13**, 697 (2011).
[82] V. Garzó and A. Santos, *Kinetic Theory of Gases in Shear Flows Nonlinear Transport* (Kluwer, Dordrecht, 2003).
[83] S.-H. Chong, M. Otsuki, and H. Hayakawa, Prog. Theor. Phys. Suppl. **184**, 72 (2010).
[84] S.-H. Chong, M. Otsuki, and H. Hayakawa, Phys. Rev. E. **81**, 041130 (2010).
[85] H. Hayakawa and M. Otsuki, Phys. Rev. E **88**, 032117 (2013).
[86] M. Abramowitz and I. A. Stegun, *Handbook of Mathematical Functions: With Formulas, Graphs, and Mathematical Tables* (Dover, New York, 1964).